Letter | Editors' Suggestion

Free-form acoustic topological waveguides enabled by topological lattice defects

Yin Wang,[1] Yong Ge,[1] Yu-Jing Lu,[1] Shuai Gu,[1] Yi-Jun Guan,[1] Qiao-Rui Si,[1] Shou-Qi Yuan,[1] Qiang Wang,[2,*] Hong-Xiang Sun,[1,3,†] and Haoran Xue[4,‡]

[1]*Research Center of Fluid Machinery Engineering and Technology, School of Physics and Electrical Engineering, School of Computer Science and Communication Engineering, Jiangsu University, Zhenjiang 212013, China*

[2]*School of Physics, Collaborative Innovation Center of Advanced Microstructures, Nanjing University, Nanjing, Jiangsu 210093, China*

[3]*State Key Laboratory of Acoustics, Institute of Acoustics, Chinese Academy of Sciences, Beijing 100190, China*

[4]*Department of Physics, The Chinese University of Hong Kong, Shatin, Hong Kong SAR, China*

(Received 28 January 2024; revised 20 April 2024; accepted 26 April 2024; published 15 May 2024)

The emerging field of topological acoustics provides exciting possibilities for controlling sound propagation with extraordinary robustness. Conventional topological acoustic waveguides built from topological edge states, which arise solely from the nontrivial topology in the momentum space, usually have restricted shapes due to their crystalline structures. Here, we show that, using an acoustic topological system with both nontrivial topologies in the real and momentum spaces, free-form acoustic topological waveguides can be constructed. These topological waveguides support disclination-localized states, caused by the interplay between topological lattice defects and the valley-Hall topology. As demonstrated in our simulations and experiments, such disclination waveguides can take arbitrary shapes and form open arcs within the lattice, which are not possible for previous crystalline acoustic topological waveguides. Furthermore, by increasing the number of topological lattice defects, we can realize more than one topological waveguide in one lattice. They join at the topological lattice defect and form a topological waveguide network, enabling more complicated functionalities such as beam splitting. Our results point to a promising direction for free-form acoustic topological devices with the advantages of embedded forms, easy cascading, and high robustness.

DOI: 10.1103/PhysRevB.109.L180101

Acoustic systems with nontrivial band topology, which support robust sound transport, have attracted great attention in recent years [1,2]. In particular, intense efforts have been devoted to studying different types of crystalline topological phases for sound, such as the quantum Hall phase [3–8], quantum spin-Hall phase [9–15], valley-Hall phase [16–23], and higher-order topological phase [24–34]. In these topological phases, on the one hand, the crystalline structure is an important prerequisite for defining the band structure in the momentum space, based on which nontrivial topology can be created. On the other hand, the form of the topological waveguiding channels in the real space is highly restricted by the crystalline structure. To maintain the periodicity of the system, a topological waveguide can only be designed to follow certain paths according to the crystalline symmetries and terminate at external boundaries, which poses great limitations on the tunability and functionality of a topological acoustic system.

Different from the momentum space band topology, topological lattice defects (TLDs) are lattice imperfections in the real space. Once generated, they cannot be removed by local perturbations due to their nontrivial real-space topological configurations [35]. Additionally, TLDs can interplay with nontrivial band topology, leading to protected topological states bound to the defects instead of the boundaries [36]. Since TLDs are noncrystalline in nature, the form of these topological states in the real space is much less constrained compared to the form of those in crystalline topological systems, which makes the TLD-induced topological states suitable for free-form waveguiding [37–43].

From the experimental perspective, classical-wave systems, such as phononic/photonic crystals and metamaterials, provide ideal platforms to study TLDs and their interplay with band topology. In classical-wave systems, TLDs can be created and manipulated almost at will owing to the high controllability in structural design and fabrication. Together with the rapid development of band topology in classical-wave systems, various interesting phenomena induced by the interplay between TLDs and band topology have been observed in recent years [36,44–50]. For example, by introducing a screw dislocation into a three-dimensional acoustic topological insulator [45,46], one-dimensional topological states bound to the dislocation have been realized. In two-dimensional topological systems, dislocations can also induce trapped states [44,47], as demonstrated in a mechanical system. In addition to dislocations, disclinations can also be constructed in classical-wave systems [48,49], which are shown to host fractional charges in topological crystalline metamaterials. Furthermore, when disclinations are incorporated into a valley acoustic crystal, a valley-Hall domain wall supporting topological transport can be created [50]. Such a domain wall is

*q.wang@nju.edu.cn
†jsdxshx@ujs.edu.cn
‡haoranxue@cuhk.edu.hk

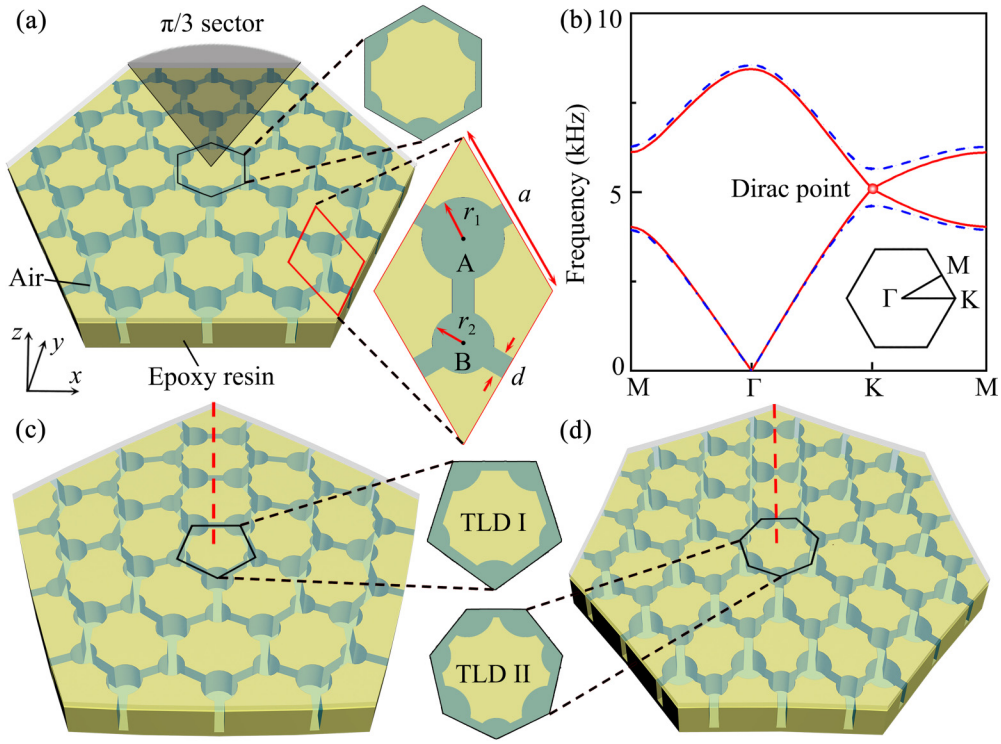

FIG. 1. (a) Schematic of a honeycomb-lattice acoustic crystal. The shaded gray region represents a $\pi/3$ sector. The two insets indicate the unit cells. (b) Simulated bulk dispersions of two honeycomb-lattice acoustic crystals with $r_1 = r_2 = 4.9$ mm (red solid lines), and $r_1 = 5.6$ mm and $r_2 = 4.2$ mm (blue dashed lines). The height of the acoustic crystal is 8.5 mm. (c) and (d) Schematics of a pentagonal acoustic crystal by deleting a $\pi/3$ sector [the gray shaded region in (a)] in the original honeycomb-lattice acoustic crystal (c) and a heptagonal acoustic crystal by inserting a $\pi/3$ sector [the gray shaded region in (a)] in the original honeycomb-lattice acoustic crystal (d). The two insets in the middle regions are two types of TLDs, labeled as TLD I and TLD II, and the red dashed lines denote the disclinations.

terminated by TLDs and its shape can be freely engineered, making it an ideal candidate for a free-form waveguide.

In this Letter, we propose a series of acoustic topological waveguides embedded with different types of disclinations which are constructed by introducing the TLDs into an acoustic valley-Hall system. The disclinations not only support robust transport of sound, but also can be optionally terminated at any location of the bulk, which effectively overcomes the limitation of forming loops or ending at external boundaries for previously demonstrated domain walls. More importantly, we go beyond the limitations in previous works [50] where the topological waveguides only have simple shapes and are terminated by just two TLDs. Specifically, we realize topological waveguides with letter-like shapes W, I, and N. By increasing the number of the TLDs, we also construct complex topological waveguide networks in irregular shapes such as an arrow and a Chinese character in which the robust topological sound transports present the patterns of the disclinations. Therefore, our results demonstrate the full ability of using TLD-induced topological states for free-form waveguiding.

As schematically shown in Fig. 1(a), we design a honeycomb-lattice acoustic crystal (with the lattice constant $a = 28.5$ mm) composed of coupled air cavities surrounded by hard walls. Each unit cell (see the lower-right inset) consists of two airborne cylindrical cavities (denoted as A and B) connected by thin channels filled with air. The radii of the airborne cavities are denoted by r_1 and r_2, respectively, and the width of the connecting channel is $d = 3.0$ mm. Throughout this Letter, we use the software COMSOL MULTIPHYSICS to compute the eigenstates and field distributions. In the simulations, the external boundaries are set as plane-wave radiation boundaries, and the parameters of air are density $\rho = 1.25$ kg/m^3 and sound speed $c = 343$ m/s.

Figure 1(b) shows the bulk dispersions of this acoustic crystal with different values of r_1 and r_2. We can see that there exists a pair of Dirac points at the K and K' valleys in the band structure when $r_1 = r_2 = 4.9$ mm (see the red solid curves). However, when the values of r_1 and r_2 are different ($r_1 = 5.6$ mm and $r_2 = 4.2$ mm), the inversion symmetry of the lattice is broken, lifting the degeneracy at the two valleys (see the blue dashed curves). This gapped phase is known as a valley-Hall phase, in which the bulk bands carry opposite Berry curvature around the two valleys and edge states with their propagation directions locked to the valleys emerge at the interface between two domains with swapped r_1 and r_2 (see the Supplemental Material [51] and also Refs. [52,53] therein).

Starting from the above crystalline valley-Hall acoustic crystal, we now describe the procedure to induce the TLDs. As illustrated in Fig. 1(a), by deleting (inserting) a $\pi/3$ sector (see the gray shaded region) in the acoustic crystal, we can obtain a pentagonal (heptagonal)-shaped acoustic crystal

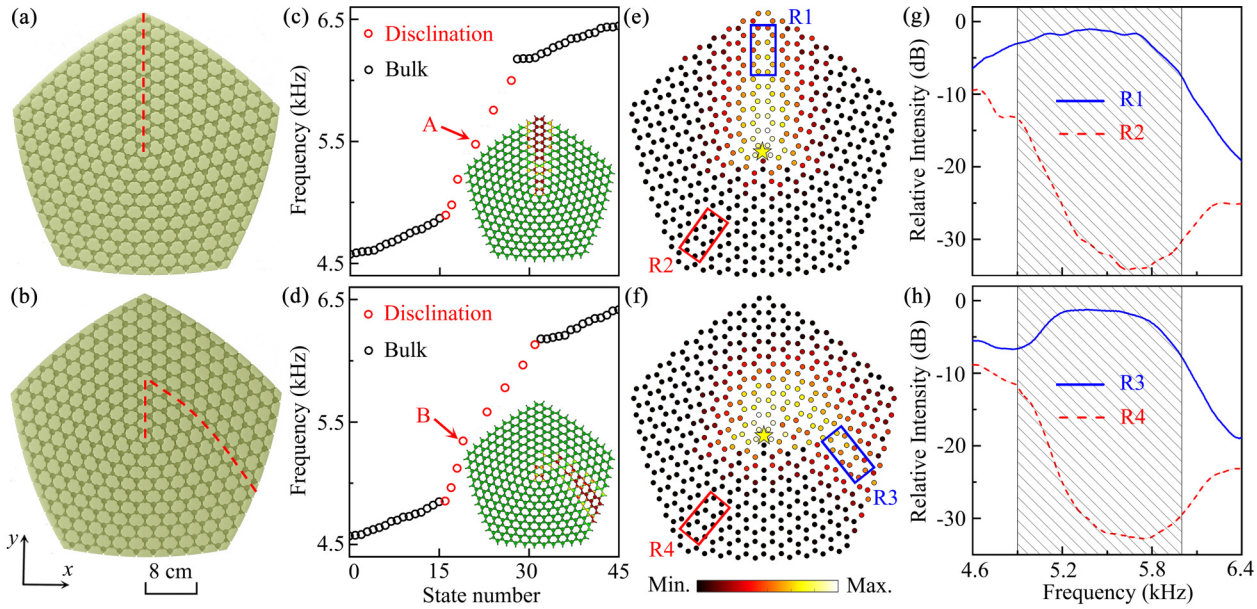

FIG. 2. (a) and (b) Photographs of two pentagonal acoustic crystals with the (a) straight and (b) bent disclinations marked by the red dashed lines. (c) and (d) Simulated eigenfrequency spectra for two pentagonal acoustic crystals with the (c) straight and (d) bent disclinations. The red and black open circles represent edge states in the disclination and bulk, respectively. (e) and (f) Measured acoustic intensity eigenstates ($|p|^2$) at the points (e) A and (f) B. The yellow stars at the center of the TLD represent dipole sound sources. (g) and (h) Measured relative intensity spectra sampled in the disclinations (the blue open rectangles R1 and R3) and bulk (the red open rectangles R2 and R4) of the pentagonal acoustic crystals with the (g) straight and (h) bent disclinations. The black shaded regions are the bulk band gap in (c) and (d).

[shown in Figs. 1(c) and 1(d)]. Here, the positions of the cavities in the newly generated acoustic crystals are optimized by the molecular dynamics simulator LAMMPS [50,54] to ensure the honeycomb structure is maintained locally away from the TLDs. As can be seen in Figs. 1(c) and 1(d), there are TLDs at the center of the acoustic crystals, which consist of either five or seven connecting channels, different from the geometry of hexagons (with six connecting channels) in the rest of the acoustic crystal. Moreover, there also exist disclination lines (red dashed lines) in the acoustic crystals, one end of which is fixed to the TLDs. Taking a closer look, we can immediately find that the cavities on two sides of the disclinations have the same radius, which means the disclinations can act as valley-Hall-type domain walls and support valley-Hall-like edge states. This observation is further validated by a theoretical analysis based on the effective Dirac Hamiltonian, as detailed in the Supplemental Material [51].

To verify the existence of the disclination states and study their robustness, we compute the eigenfrequencies and eigenstates for two pentagonal acoustic crystals with straight and bent disclinations, whose photographs are shown in Figs. 2(a) and 2(b), respectively. As shown in Fig. 2(c), for the pentagonal acoustic crystal with a straight disclination, there exist six states inside the band gap (of the original crystalline acoustic crystal), which are confirmed to be localized around the disclination according to their eigenprofiles. For the pentagonal acoustic crystal with a bent disclination, similar in-gap disclination states can also be found [Fig. 2(d)]. The results for the heptagonal acoustic crystals are similar and are given in the Supplemental Material [51].

Next, we conduct experiments to measure the intensity distributions excited by a point source placed at the center of the TLD for the pentagonal acoustic crystals. A detailed description of the experimental setup is can be found in the Supplemental Material [51]. As shown in Figs. 2(e) and 2(f), the topological disclination states can transmit through the disclination of both types of pentagonal acoustic crystals with high performance. Moreover, we experimentally measure the relative intensity spectra in the disclinations (R1 and R3) and bulk (R2 and R4) of both pentagonal acoustic crystals based on

$$I = 10\log\left(\frac{|p_{\mathrm{m}}|^2}{|p_{\mathrm{s}}|^2}\right), \tag{1}$$

where p_{m} represents the average value of the measured pressure amplitude of each point in the regions R1–R4, and p_{s} is the measured pressure amplitude at the position of the sound source. As shown in Figs. 2(g) and 2(h), in the bulk band gap (black shaded regions), there exists an obvious intensity dip in the bulk for both types of pentagonal acoustic crystals. However, the measured relative intensities are larger than -7 dB in the disclinations, showing high waveguiding performance. Additionally, the measured relative intensity spectra in the straight disclination are very similar to those in the bent disclination, showing robust topological sound transport in the pentagonal acoustic crystal with the TLD.

Based on the pentagonal and heptagonal acoustic crystals with TLDs, we can construct another type of topological waveguides embedded with various distinctive disclinations, which cannot be realized by the traditional topological waveguides. As the first example, we design three types of

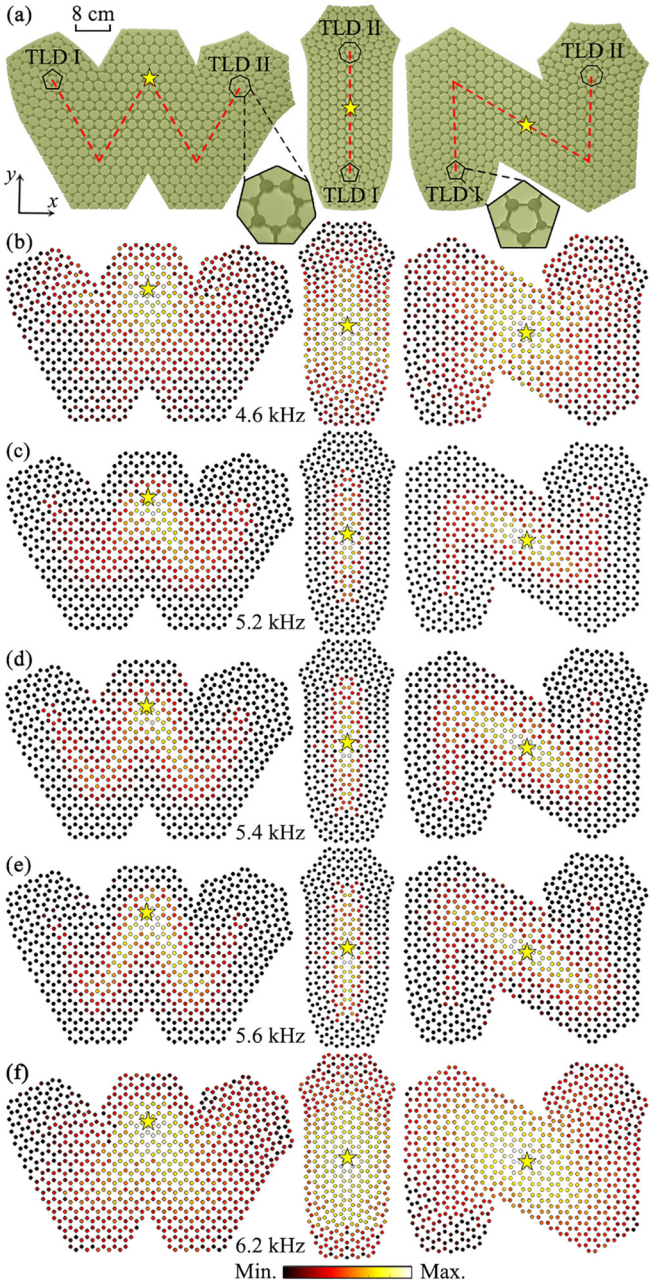

FIG. 3. (a) Photographs of three topological waveguides embedded with W-, I-, and N-shaped disclinations. The insets show the two types of topological lattice defects. The red dashed lines and yellow stars denote the disclinations and sound sources, respectively. (b)–(f) Measured intensity distributions in the three samples at (b) 4.6 kHz, (c) 5.2 kHz, (d) 5.4 kHz, (e) 5.6 kHz, and (f) 6.2 kHz.

topological waveguides embedded with the three letters W-, I-, and N-shaped disclinations by using a pentagonal acoustic crystal with TLD I and a heptagonal acoustic crystal with TLD II [Fig. 3(a)]. It is noted that the W-, I-, and N-shaped disclinations are realized by bending the acoustic crystal in the central region, and placing a pentagonal and a heptagonal acoustic crystal with the TLDs I and II on both sides. Figures 3(b)–3(f) show the measured intensity distributions through the three topological waveguides at different frequencies, in which a point sound source is placed at the middle of the disclination. It is observed that the sound energy can transmit through the disclinations, exhibiting the profiles of the three letters W, I, and N when the excitation frequency is inside the band gap [Figs. 3(c)–3(e)]. By contrast, the sound fields are not localized around the disclinations at 4.6 kHz [Fig. 3(b)] and 6.2 kHz [Fig. 3(f)], which are away from the band gap. The simulated intensity distributions of the topological waveguides with the W-, I-, and N-shaped disclinations are also presented in the Supplemental Material [51], and the results agree well with the experiments, showing the feasibility of the robust topological waveguides embedded with the TLDs.

Furthermore, by increasing the number of TLDs, we can realize topological waveguides embedded with more complex propagating paths. Figures 4(a) and 4(b) show two types of topological waveguides embedded with the arrow and Chinese character 人-shaped disclinations, which are constructed by three pentagonal acoustic crystals with the TLD I and one heptagonal acoustic crystal with the TLD II. Figures 4(c) and 4(d) show the measured intensity distributions through the two topological waveguides at 4.6, 5.2, 5.4, 5.6, and 6.2 kHz. We observe that, at 5.2, 5.4 and 5.6 kHz, the sound energy propagates along the disclination, passes through the heptagonal acoustic crystal with the TLD II, and finally reaches the pentagonal acoustic crystals with TLD I on both sides. In addition, the sound energy is well bound in the disclinations, and terminates in the three TLD I at three selected frequencies, whose propagating paths are shown as the shapes of the arrow and a Chinese character 人. At bulk frequencies, however, the sound propagation does not follow the disclination shapes, as can be seen from the measured intensity distributions at 4.6 and 6.2 kHz [Figs. 4(c) and 4(d)]. The simulated results for two types of topological waveguides at the selected frequencies are also presented in the Supplemental Material [51], and the simulated intensity distributions agree well with the measured ones in Figs. 4(c) and 4(d).

In principle, we can include more TLDs to achieve more complex waveguide networks. In the Supplemental Material [51], we show the designs of two more topological waveguides embedded with K- and *-shaped disclinations. Therefore, based on two types of acoustic crystals with the TLDs, we design a variety of free-form topological waveguides embedded with various disclinations to realize multifunctional robust topological sound transport.

In conclusion, we have experimentally demonstrated free-form topological waveguides embedded with various distinctive disclinations by introducing TLDs into valley-Hall-type acoustic crystals. The results show that there exist topological states bound to disclinations, whose propagation is robust against the path bends. Different from the conventional topological waveguides, the topological waveguides introduced here can be terminated inside the lattice and take almost arbitrary shapes by engineering the disclination pattern, such as the topological waveguides embedded with the letterlike shapes W, I, and N, and the irregular shapes of an arrow and a Chinese character 人 disclinations. With these advantages, the proposed free-form acoustic topological waveguides could be useful for next-generation high-performance acoustic devices.

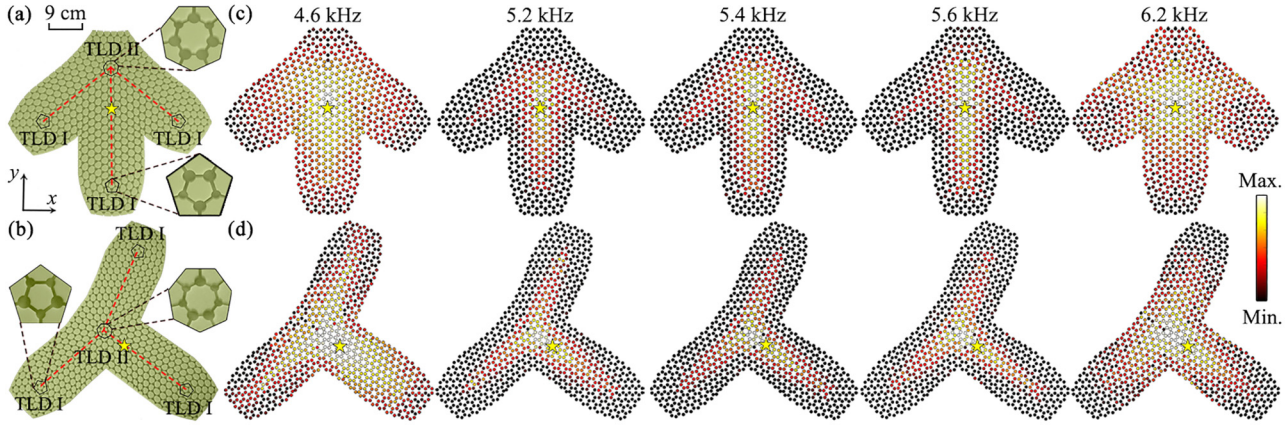

FIG. 4. (a) and (b) Photographs of two embedded topological waveguides with (a) an arrow-shaped disclination and (b) a Chinese character 人-shaped disclination. The red dashed lines and yellow stars denote the disclinations and sound sources, respectively. (c) and (d) Measured acoustic intensity distributions in the two samples at different frequencies.

This work was supported by the National Natural Science Foundation of China (Grants No. 12274183, No. 12174159, and No. 51976079), the National Key R&D Program of China (Grant No. 2020YFC1512403), the Jiangsu Qing Lan Project, and the Research Project of State Key Laboratory of Mechanical System and Vibration (Grant No. MSV202201). H.X. acknowledges support from the start-up fund and the direct grant (Grant No. 4053675) of the Chinese University of Hong Kong.

[1] G. Ma, M. Xiao, and C. T. Chan, Topological phases in acoustic and mechanical systems, Nat. Rev. Phys. **1**, 281 (2019).
[2] H. Xue, Y. Yang, and B. Zhang, Topological acoustics, Nat. Rev. Mater. **7**, 974 (2022).
[3] Z. Yang, F. Gao, X. Shi, X. Lin, Z. Gao, Y. Chong, and B. Zhang, Topological acoustics, Phys. Rev. Lett. **114**, 114301 (2015).
[4] X. Ni, C. He, X.-C. Sun, X.-p. Liu, M.-H. Lu, L. Feng, and Y.-F. Chen, Topologically protected one-way edge mode in networks of acoustic resonators with circulating air flow, New J. Phys. **17**, 053016 (2015).
[5] A. B. Khanikaev, R. Fleury, S. H. Mousavi, and A. Alu, Topologically robust sound propagation in an angular-momentum-biased graphene-like resonator lattice, Nat. Commun. **6**, 8260 (2015).
[6] Z. G. Chen and Y. Wu, Tunable topological phononic crystals, Phys. Rev. Appl. **5**, 054021 (2016).
[7] A. Souslov, B. C. Van Zuiden, D. Bartolo, and V. Vitelli, Topological sound in active-liquid metamaterials, Nat. Phys. **13**, 1091 (2017).
[8] Y. Ding, Y. Peng, Y. Zhu, X. Fan, J. Yang, B. Liang, X. Zhu, X. Wan, and J. Cheng, Experimental demonstration of acoustic Chern insulators, Phys. Rev. Lett. **122**, 014302 (2019).
[9] C. He, X. Ni, H. Ge, X.-C. Sun, Y.-B. Chen, M.-H. Lu, X.-P. Liu, and Y.-F. Chen, Acoustic topological insulator and robust one-way sound transport, Nat. Phys. **12**, 1124 (2016).
[10] Z. Zhang, Q. Wei, Y. Cheng, T. Zhang, D. Wu, and X. Liu, Topological creation of acoustic pseudospin multipoles in a flow-free symmetry-broken metamaterial lattice, Phys. Rev. Lett. **118**, 084303 (2017).
[11] B.-Z. Xia, T.-T. Liu, G.-L. Huang, H.-Q. Dai, J.-R. Jiao, X.-G. Zang, D.-J. Yu, S.-J. Zheng, and J. Liu, Topological phononic insulator with robust pseudospin-dependent transport, Phys. Rev. B **96**, 094106 (2017).
[12] S. Yves, R. Fleury, F. Lemoult, M. Fink, and G. Lerosey, Topological acoustic polaritons: Robust sound manipulation at the subwavelength scale, New J. Phys. **19**, 075003 (2017).
[13] D. Jia, H.-x. Sun, J.-p. Xia, S.-q. Yuan, X.-j. Liu, and C. Zhang, Acoustic topological insulator by honeycomb sonic crystals with direct and indirect band gaps, New J. Phys. **20**, 093027 (2018).
[14] R. E. Christiansen, F. Wang, and O. Sigmund, Topological insulators by topology optimization, Phys. Rev. Lett. **122**, 234502 (2019).
[15] W. Deng, X. Huang, J. Lu, V. Peri, F. Li, S. D. Huber, and Z. Liu, Acoustic spin-Chern insulator induced by synthetic spin–orbit coupling with spin conservation breaking, Nat. Commun. **11**, 3227 (2020).
[16] J. Lu, C. Qiu, M. Ke, and Z. Liu, Valley vortex states in sonic crystals, Phys. Rev. Lett. **116**, 093901 (2016).
[17] J. Lu, C. Qiu, L. Ye, X. Fan, M. Ke, F. Zhang, and Z. Liu, Observation of topological valley transport of sound in sonic crystals, Nat. Phys. **13**, 369 (2017).
[18] J. Lu, C. Qiu, W. Deng, X. Huang, F. Li, F. Zhang, S. Chen, and Z. Liu, Valley topological phases in bilayer sonic crystals, Phys. Rev. Lett. **120**, 116802 (2018).
[19] Z. Zhang, Y. Tian, Y. Wang, S. Gao, Y. Cheng, X. Liu, and J. Christensen, Directional acoustic antennas based on valley-Hall topological insulators, Adv. Mater. **30**, 1803229 (2018).
[20] M. Wang, W. Zhou, L. Bi, C. Qiu, M. Ke, and Z. Liu, Valley-locked waveguide transport in acoustic heterostructures, Nat. Commun. **11**, 3000 (2020).
[21] Z. Tian, C. Shen, J. Li, E. Reit, H. Bachman, J. E. Socolar, S. A. Cummer, and T. Jun Huang, Dispersion tuning and route reconfiguration of acoustic waves in valley topological phononic crystals, Nat. Commun. **11**, 762 (2020).

[22] H. Qu, X. Liu, and G. Hu, Topological valley states in sonic crystals with Willis coupling, Appl. Phys. Lett. **119**, 051903 (2021).
[23] D. Jia, Y. Ge, H. Xue, S. Q. Yuan, H. X. Sun, Y. Yang, X. J. Liu, and B. Zhang, Topological refraction in dual-band valley sonic crystals, Phys. Rev. B **103**, 144309 (2021).
[24] H. Xue, Y. Yang, F. Gao, Y. Chong, and B. Zhang, Acoustic higher-order topological insulator on a kagome lattice, Nat. Mater. **18**, 108 (2019).
[25] X. Ni, M. Weiner, A. Alu, and A. B. Khanikaev, Observation of higher-order topological acoustic states protected by generalized chiral symmetry, Nat. Mater. **18**, 113 (2019).
[26] X. Zhang, H.-X. Wang, Z.-K. Lin, Y. Tian, B. Xie, M.-H. Lu, Y.-F. Chen, and J.-H. Jiang, Second-order topology and multidimensional topological transitions in sonic crystals, Nat. Phys. **15**, 582 (2019).
[27] H. Xue, Y. Yang, G. Liu, F. Gao, Y. Chong, and B. Zhang, Realization of an acoustic third-order topological insulator, Phys. Rev. Lett. **122**, 244301 (2019).
[28] X. Zhang, B.-Y. Xie, H.-F. Wang, X. Xu, Y. Tian, J.-H. Jiang, M.-H. Lu, and Y.-F. Chen, Dimensional hierarchy of higher-order topology in three-dimensional sonic crystals, Nat. Commun. **10**, 5331 (2019).
[29] M. Weiner, X. Ni, M. Li, A. Alù, and A. B. Khanikaev, Demonstration of a third-order hierarchy of topological states in a three-dimensional acoustic metamaterial, Sci. Adv. **6**, eaay4166 (2020).
[30] X. Ni, M. Li, M. Weiner, A. Alù, and A. B. Khanikaev, Demonstration of a quantized acoustic octupole topological insulator, Nat. Commun. **11**, 2108 (2020).
[31] H. Xue, Y. Ge, H.-X. Sun, Q. Wang, D. Jia, Y.-J. Guan, S.-Q. Yuan, Y. Chong, and B. Zhang, Observation of an acoustic octupole topological insulator, Nat. Commun. **11**, 2442 (2020).
[32] Y. Qi, C. Qiu, M. Xiao, H. He, M. Ke, and Z. Liu, Acoustic realization of quadrupole topological insulators, Phys. Rev. Lett. **124**, 206601 (2020).
[33] L.-Y. Zheng and J. Christensen, Dirac hierarchy in acoustic topological insulators, Phys. Rev. Lett. **127**, 156401 (2021).
[34] H. Chen, H. Zhang, Q. Wu, Y. Huang, H. Nguyen, E. Prodan, X. Zhou, and G. Huang, Creating synthetic spaces for higher-order topological sound transport, Nat. Commun. **12**, 5028 (2021).
[35] N. D. Mermin, The topological theory of defects in ordered media, Rev. Mod. Phys. **51**, 591 (1979).
[36] Z.-K. Lin, Q. Wang, Y. Liu, H. Xue, B. Zhang, Y. Chong, and J.-H. Jiang, Topological phenomena at defects in acoustic, photonic and solid-state lattices, Nat. Rev. Phys. **5**, 483 (2023).
[37] H. Miyazaki, M. Hase, H. T. Miyazaki, Y. Kurokawa, and N. Shinya, Photonic material for designing arbitrarily shaped waveguides in two dimensions, Phys. Rev. B **67**, 235109 (2003).
[38] K. Edagawa, S. Kanoko, and M. Notomi, Photonic amorphous diamond structure with a 3D photonic band gap, Phys. Rev. Lett. **100**, 013901 (2008).
[39] M. Florescu, S. Torquato, and P. J. Steinhardt, Designer disordered materials with large, complete photonic band gaps, Proc. Natl. Acad. Sci. USA **106**, 20658 (2009).
[40] J.-K. Yang, C. Schreck, H. Noh, S.-F. Liew, M. I. Guy, C. S. O'Hern, and H. Cao, Photonic-band-gap effects in two-dimensional polycrystalline and amorphous structures, Phys. Rev. A **82**, 053838 (2010).
[41] S. Imagawa, K. Edagawa, K. Morita, T. Niino, Y. Kagawa, and M. Notomi, Photonic band-gap formation, light diffusion, and localization in photonic amorphous diamond structures, Phys. Rev. B **82**, 115116 (2010).
[42] W. Man, M. Florescu, E. P. Williamson, Y. He, S. R. Hashemizad, B. Y. Leung, D. R. Liner, S. Torquato, P. M. Chaikin, and P. J. Steinhardt, Isotropic band gaps and freeform waveguides observed in hyperuniform disordered photonic solids, Proc. Natl. Acad. Sci. USA **110**, 15886 (2013).
[43] M. Florescu, P. J. Steinhardt, and S. Torquato, Optical cavities and waveguides in hyperuniform disordered photonic solids, Phys. Rev. B **87**, 165116 (2013).
[44] F.-F. Li, H.-X. Wang, Z. Xiong, Q. Lou, P. Chen, R.-X. Wu, Y. Poo, J.-H. Jiang, and S. John, Topological light-trapping on a dislocation, Nat. Commun. **9**, 2462 (2018).
[45] H. Xue, D. Jia, Y. Ge, Y. J. Guan, Q. Wang, S. Q. Yuan, H. X. Sun, Y. D. Chong, and B. Zhang, Observation of dislocation-induced topological modes in a three-dimensional acoustic topological insulator, Phys. Rev. Lett. **127**, 214301 (2021).
[46] L. Ye, C. Qiu, M. Xiao, T. Li, J. Du, M. Ke, and Z. Liu, Topological dislocation modes in three-dimensional acoustic topological insulators, Nat. Commun. **13**, 508 (2022).
[47] Z.-K. Lin, Y. Wu, B. Jiang, Y. Liu, S.-Q. Wu, F. Li, and J.-H. Jiang, Topological Wannier cycles induced by sub-unit-cell artificial gauge flux in a sonic crystal, Nat. Mater. **21**, 430 (2022).
[48] Y. Liu, S. Leung, F.-F. Li, Z.-K. Lin, X. Tao, Y. Poo, and J.-H. Jiang, Bulk–disclination correspondence in topological crystalline insulators, Nature (London) **589**, 381 (2021).
[49] C. W. Peterson, T. Li, W. Jiang, T. L. Hughes, and G. Bahl, Trapped fractional charges at bulk defects in topological insulators, Nature (London) **589**, 376 (2021).
[50] Q. Wang, H. Xue, B. Zhang, and Y. D. Chong, Observation of protected photonic edge states induced by real-space topological lattice defects, Phys. Rev. Lett. **124**, 243602 (2020).
[51] See Supplemental Material at http://link.aps.org/supplemental/10.1103/PhysRevB.109.L180101 for the band dispersion of the crystalline acoustic crystal, the effective theory, the experimental details, the numerical results for heptagonal acoustic crystals with straight and bent disclinations, the simulated intensity distributions of topological waveguides embedded with W-, I-, and N-shaped disclinations, the simulated intensity distributions through topological waveguides embedded with arrow and Chinese character 人-shaped disclinations, and the design and performance of topological waveguides embedded with K- and *-shaped disclinations, which includes Refs. [52,53].
[52] P. E. Lammert and V. H. Crespi, Topological phases in graphitic cones, Phys. Rev. Lett. **85**, 5190 (2000).
[53] P. E. Lammert and V. H. Crespi, Graphene cones: Classification by fictitious flux and electronic properties, Phys. Rev. B **69**, 035406 (2004).
[54] S. Plimpton, Fast parallel algorithms for short-range molecular dynamics, J. Comput. Phys. **117**, 1 (1995).